

s . T X s s s (. . , s -
 s) , X fl fi s
 (. . , l ss, f s) f 3DG. B s s, -
 3DG ll s f l l
 (. . , s , s , s f l). H , s f s
 l l s s , f s , l N f
 ll s s l ll f
 , s s l 3DG s s l f -
 s s s f s f s fi f l s 17,18 .
 H , s f ss l l s ,
 s l l f s s 3DG
 l s s s l f s 19 .
 S l l s l (SLM), s -
 f (AM) l , s l l s f f
 f s s / s X - s l (3D) l l s
 s f l X s , ffi
 fi X l f in-situ f l . T , s
 s s SLM s s s f T ll s 20 ,
 s l ss ll s 21 , N ll s 22 . C s s l s f l /
 s s f l - s s s - f - -
 s s l s . C N s s ,
 s s s l s s f
 CVD l s l (< 0.001 .%)
 ss s l f , -
 l s l l s 23 . W l N s
 s l l (> 0.1 .%) 17 , fi s
 f s f X ss 24 . H , -
 s SLM f s s ll s f s ffi
 f s l s s s l
 fl s l s l
 (1000–1100). F f s s s ff l s
 SLM s s ll f ll s 25 .
 T l s , f fi s s
 f s l - 3DG/ (3DG/C) s -
 s SLM s l s CVD f
 . A ll- s - s l s
 ll s SLM f s l l -
 s f , s ll s s s3(l) 45.13, . l 20-37

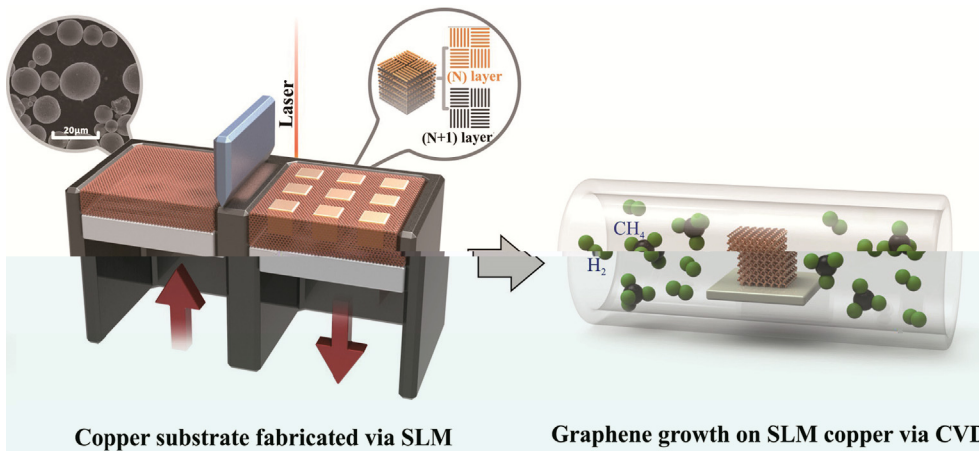


Fig. 1. SLM of copper substrate and in-situ CVD growth of graphene on SLM copper substrate.

ASTM B193-2002 (2010) and ASTM E1461-2013 (2013) standards were used for the mechanical testing. The tensile strength and elongation at break were measured using a universal testing machine (LFA457, GOM) with a load cell of 500 N. The microhardness was measured using a Vickers microhardness tester (VNA, AVEVA) with a load of 10 mN. The surface morphology was characterized using a scanning electron microscope (SEM, ZEISS) with a magnification of 1000x. The chemical composition was analyzed using an energy-dispersive X-ray (EDS) spectrometer (EDS, ZEISS). The Raman spectra were recorded using a Raman spectrometer (SENTERRA, BOMTECH) with a laser power of 500 mW and a wavelength of 532 nm. The Raman spectra were fitted using Origin software. The G and 2D bands were deconvoluted into four Lorentzian peaks. The intensity ratio of the G and 2D bands (I_{2D}/I_G) was used to evaluate the defect density of the graphene. The defect density was calculated using the following equation:

$$D = \frac{I_{D+D'}}{I_G} \times \frac{1}{L} \times \frac{1}{\sqrt{A}}$$

where D is the defect density, $I_{D+D'}$ is the intensity of the D and D' bands, I_G is the intensity of the G band, L is the length of the graphene sheet, and A is the area of the graphene sheet.

3. Results and discussion

3.1. Formation of SLM copper

3.1.1. SLM manufacturing of copper under different line energy densities

The SLM process parameters were varied to achieve different line energy densities. The laser power and scanning speed were the main parameters that affect the line energy density. The line energy density was calculated using the following equation:

$$LE = \frac{P}{v}$$

where LE is the line energy density, P is the laser power, and v is the scanning speed.

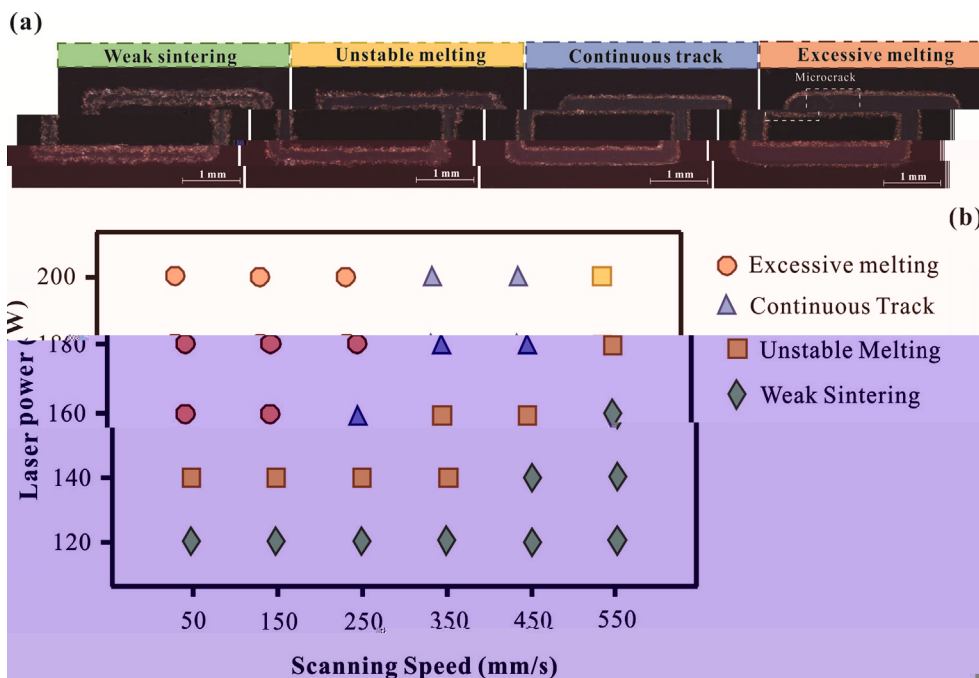


Fig. 2. (a) SEM images of SLM copper tracks under different conditions. (b) Relationship between Laser power and Scanning Speed for different SLM conditions.

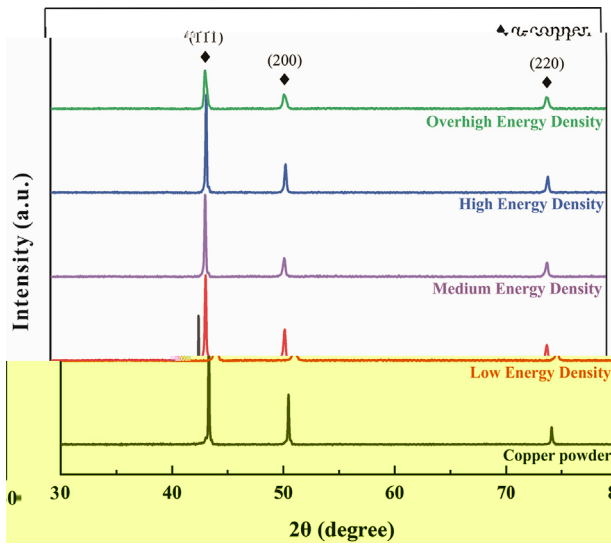


Fig. 3. RD patterns of copper powder at different energy densities. The peaks are indexed to the (111), (200) and (220) planes of copper powder.

3.1.2. Formation of anisotropic microstructure under different volumetric energy density

The microstructure of the SLM copper powder is shown in Fig. 4. The microstructure is highly anisotropic, with a clear layer structure. The layer structure is formed due to the layer-by-layer deposition of the powder. The layer structure is characterized by the presence of inter-layer voids and pores with cracks. The inter-layer voids are formed due to the incomplete fusion of the powder particles in the inter-layer region. The pores with cracks are formed due to the evaporation of the solvent during the SLM process. The inter-layer voids and pores with cracks are shown in Fig. 4(a) and (b). The inter-layer voids are shown in Fig. 4(a) and (b). The pores with cracks are shown in Fig. 4(a) and (b). The inter-layer voids and pores with cracks are shown in Fig. 4(a) and (b).

The microstructure of the SLM copper powder is shown in Fig. 4. The microstructure is highly anisotropic, with a clear layer structure. The layer structure is formed due to the layer-by-layer deposition of the powder. The layer structure is characterized by the presence of inter-layer voids and pores with cracks. The inter-layer voids are formed due to the incomplete fusion of the powder particles in the inter-layer region. The pores with cracks are formed due to the evaporation of the solvent during the SLM process. The inter-layer voids and pores with cracks are shown in Fig. 4(a) and (b). The inter-layer voids are shown in Fig. 4(a) and (b). The pores with cracks are shown in Fig. 4(a) and (b). The inter-layer voids and pores with cracks are shown in Fig. 4(a) and (b).

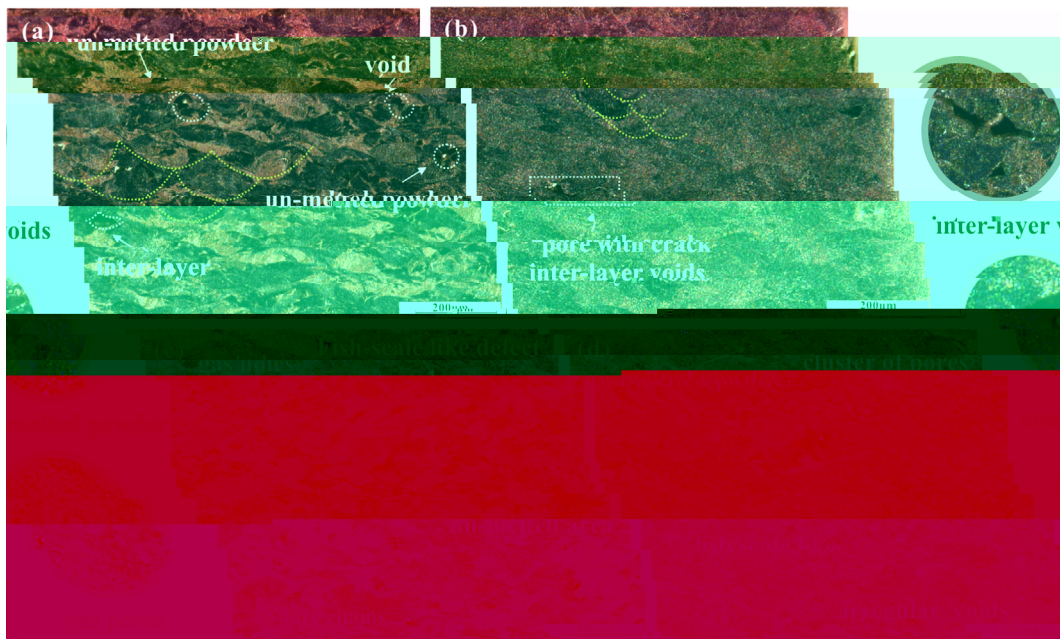


Fig. 4. SEM micrographs of SLM copper powder. (a) shows the powder surface with labels for 'un-melted powder', 'void', 'inter-layer voids', and 'inter-layer'. (b) shows a cross-section of the powder with labels for 'un-melted powder', 'pore with crack', 'inter-layer voids', and 'inter-layer voids'. Both images include a 200 μm scale bar.

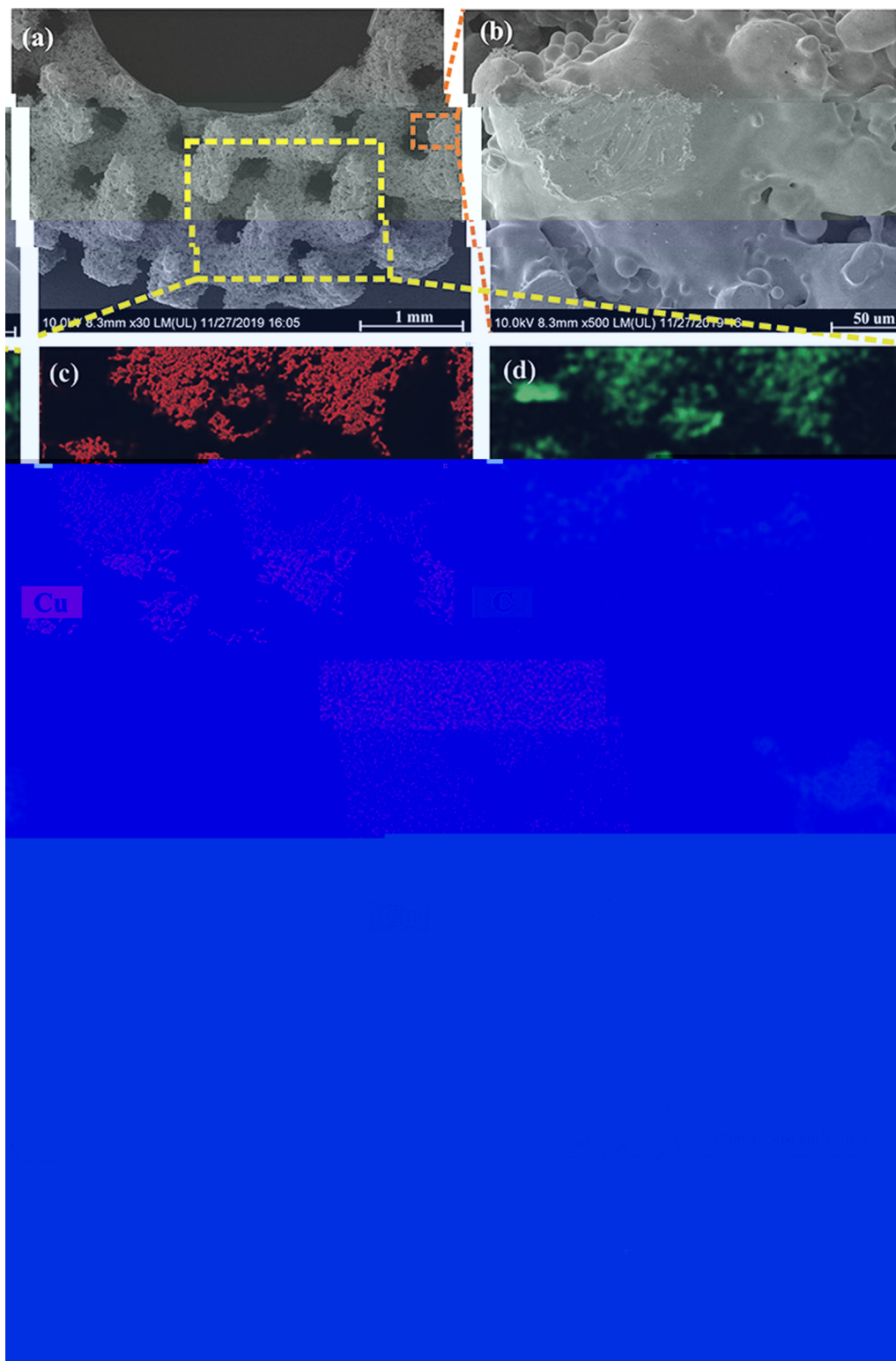


Fig. 8. (a) SEM image of 3DG/Cu porous scaffold at 30x magnification. (b) SEM image of 3DG/Cu porous scaffold at 500x magnification. (c) EDS elemental map for Copper (Cu). (d) EDS elemental map for Carbon (C).

3.4. Thermal property and EMI shielding effectiveness of 3DG/Cu porous scaffolds

The thermal stability of the 3DG/Cu porous scaffolds was evaluated by TGA. The TGA curves of 3DG/Cu porous scaffolds with different Cu content (0, 10, 20, 30, 40, 50, 60, 70, 80, 90, 100 wt%) are shown in Fig. 9. The TGA curves show that the 3DG/Cu porous scaffolds exhibit good thermal stability. The weight loss of the 3DG/Cu porous scaffolds is mainly due to the decomposition of the 3DG. The weight loss of the 3DG/Cu porous scaffolds is about 26.8% at 1000 °C. The weight loss of the 3DG/Cu porous scaffolds is about 14.8% at 1000 °C.

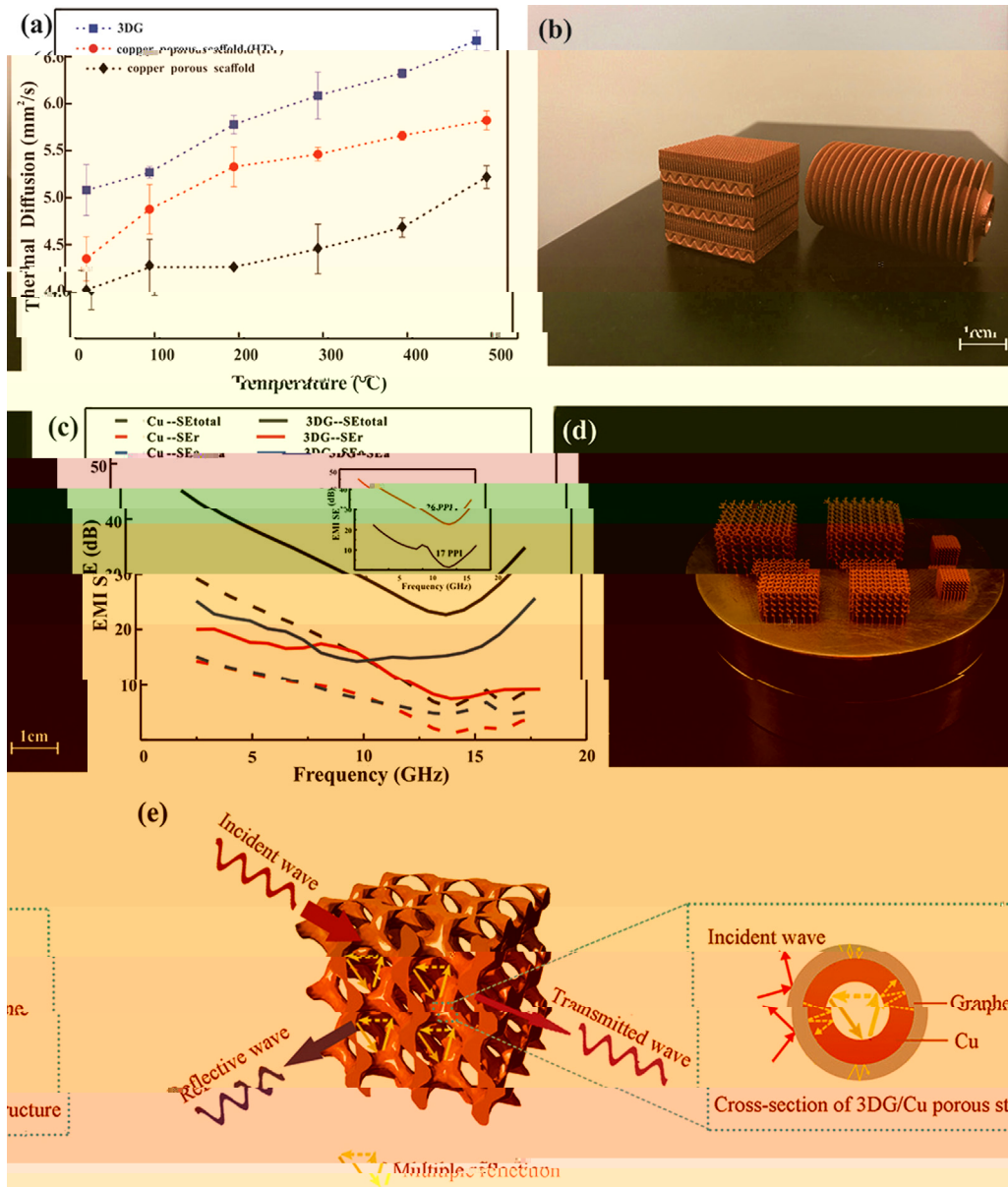


Fig. 9. (a) Thermal Diffusion (mm²/s) vs Temperature (°C) for 3DG, copper porous scaffold, and copper porous scaffold. (b) 3D model of a porous structure. (c) EMI SE (dB) vs Frequency (GHz) for Cu--SEtotal, 3DG--SEtotal, Cu--SEr, 3DG--SEr, Cu--SEp, and 3DG--SEp. (d) 3D model of a porous structure on a substrate. (e) Schematic of wave interaction with a porous structure showing incident, reflective, and transmitted waves, and a cross-section of 3DG/Cu porous structure.

Table 1

Coating materials	Substrate	Method	Maximum shielding efficiency (dB)	Improvement of thermal property (%)	Ref
G	G	I	37	-	50
G	PS	H	29.3	-	56
G	PMMA	S	19	-	57
C /G	/C	S	-	8.5	58
G	N	F	-	554	59
G	C -N	E	20	-	60
G	C	P	-	2.4	61
G	C	F	47	6.3	62
G	C	CVD + SLM	47.8	27	T s

Note: () -PPMA, () -PS.

Declaration of Competing Interest

T s l s fl f s
l f s .

Acknowledgement

T s f ll l fi l s f
N l N l S F f C (N . 51671091, N .
51902295, N . 51675496). T
F l R s F s f C l U s s, C
U s f G s s (W) (N . (N . CUG170677) H
P N l S F (N . 2019 CFB264).

Appendix A. Supplementary data

S l s l f l s://
. /10.1016/ s s .2020.105904.

References

1 B RG, N N, M s K, M S. G : s l l f f
s s ss .P M S 2018;91:24-69.
2 B l AA, G s S, B W, C l, T l D, M F, l S
f s l l N L 2008;8(3):902-7.
3 L , H, C s M, P l H, P O, S l G, l I s X -
f l f s s f l s f f i l s l
s s. ACS A l M I f s 2016;8(36):24112-22.
4 K M, K J, J B, C , K JH, A JH. G - s - s l
s s f l l s. ACS N 2017;11(8):7950-7.
5 P , C M, H M, T M, , L D. P
s l f f - s l l l l
A l C l B 2020;262:118266-76.
6 L J, W, C LL, J SH, W G, L, l F l C-G f
l s s l .C s P A
2017;101:50-8.
7 HQ, L SW, C LH, J SH, H HQ. S l f -
- f l - s. J M C A
2018;6(42):21216-24.
8 D l s TM, S P, D s P, K J, K M, A s T, l 3D -
- s- l l l l l l s f s l s
l l l s f H . P C . P s 2017;1(4):467-70.
9 Q L, L L. T s l s l s s f l s s f l s X s .
ss l f l s f l s s f l s X s .
RSC A 2014;4(72):38273-80.
10 D , H L SP, N, W X JG. 3D X -
M S2 s : P s l s -
f .C s P A 2016;90:424-32.
11 L L, W, S CO, H MK, HL, D W, l S l f ss l -s ll
- f ll s s 3D f l s fi EM -
s f .A F M 2018. s:// . /10.1002/ f .
201803938.
12 L J, P , C, R G, , N l s D, l G
s S O2 s s f l s. ACS N
2013;7(7):6001-6.
13 J SH, A l S, G A. L - s ll l s s s f l
l s. A C I E 2017;56:15520-38.
14 I , T , S K, K s M, T s T, T K, l. T -
s l s s l - s l
s. PCCP 2018;20(9):6024-33.
15 S K, D N, M ll C, V s l N, E l J. T ll l
l J E l S 2002;149(8):370-7.
16 C H, S M, S WH, L G, H , Q, l P f l 3D
X s f s s. S ll 2011;7(22):3163-8.
17 K s H, G X M, J s l, H J, W C, C M. U l -
f s l f - s l - s l
. M 2019;1(4):1077-87.
18 S Q, F , L W, L H, L , l C - l l
- s ll l f s f l - f - l l
f l s l .A M 2017;29(31):1701583-90.
19 , G C, L, T H, D, W , l. T s ll f -
f l f s s s f
s. ACS N 2019. s:// . /10.1021/ s .9 08191.
20 C C, H , B , N J, C S, L F, l 3D s T 6A l 4V :
ff s f l s f l ;
l l M D s 2019;175:107824-33.
21 S š č J, B ž č D. T ff f NB s f l -
s f 316L s ll s l s l s SLM. S f C
T l 2016;307:407-17.

22 R DC, HB, L J, L SJ, J W, R, l M s
f T-N ll f s l l s l .M S E A-S
2020;771:138586-95.
23 L , C W, A J, K S, N J, D, l L - s s s f - l
f fil s f l s. S 2009;324(5932):1312-4.
24 C P, R WC, G LB, L BL, P SE, C HM. T - s l f l l
s . N M 2011;10:424-8.
25 J SD, D s S, G ss s L, K JP, H X JV, V s l K.
I fl f s l l s ll ss s X l
. J M P ss T l 2019;270:47-58.
26 W, H L, L , T D, C Q, F , l. Eff (s l l s l
s s l , s fi
s f s s l ll . M D s 2019;170:107697-708.
27 G DD, M s W, W ss K, P R. L s f f
ll s: l s, ss s s. I M R
2013;57(3):133-64.
28 L E, T s S, C s L, F A. Eff (s l l s l (SLM)
ss s s s f 316L s
s ll s s l J M P ss T l 2017;249:255-63.
29 s , S, W , L J, W P, C , l. F f l s s f
s l s s l l s l f T 6A l 4V. A l P s A: M S
P ss 2018;124:685-98.
30 L , M, S, D W, S C. I s s
s l l s l f A l S 316L s ll s s l . M D s
2015;87:797-806.
31 L CLA, M ss S, T M, A RC, W s PJ, L PD. T ff f
f f f l s f .A M
2019;166:294-305.
32 T , K , T WQ, T J, D s s M, M l D, l. R l -
s s f α/β f l -
s l T -6A l 4V. S R 2016;6:26039-48.
33 K H, T P, L NH, T SB, C CK. G f s
ss f s l l T -6A l 4V s. V l
P s P 2016;11(3):183-91.
34 R fi HK, K NV, G H, S TL, S BE. M s s l
l . J M E P f 2013;22(12):3872-83.
35 T , K , T J, V s l G, P Q , G, l. A X l
s l T -6A l 4V. J A ll s C 2015;646:303-9.
36 R DA, M LE, M H , l. N l - s l
l f f f s l
f , s l l f l .A M 2011;59(10):4088-99.
37 s , f s l l s l C -2.4N -0.7S ll . J A ll s C
2018;743:258-61.
38 K S. W ll . S E 2003;23:309-48.
39 L G , G s J ff R, G s N P. E l C (111). N
L 2010;10(9):3512-6.
40 L S, C WW, C l , R ff R S. E l f
C s l l . N L 2009;9(12):4268-72.
41 W, C, W H, SQ, L. A s l l l l -f
f s f s f s. C
2020;161:479-85.
42 F AC, M JC, S V, C s C, L M, M F, l R
s f s P s R L 2006;97(18):187401-4.
43 S , G, J SH, F PC, H HQ. F l f l
- l s fi s l l
M L 2017;200:97-100.
44 J K, H, J, C J, D . F l l f
s l f f - ll f f C -N ll CNTs.
A l S f S 2014;311:351-6.
45 R š K, M l DP, A s C, M S, S š K. X ll EMI s l
l s l s l s l
- s s f s. C s P A 2018;12:475-84.
46 S B, L , W, W. C ss l - f s
l l s f š s l l f (EMI) s l . ACS
A l M I f s 2016;8(12):8050-7.
47 L N, H , D F, H , L , G (F 8.2(56020T (985)T l J.3(1)-340.5(S 0)-3254

M 2019;34(5):489–98.

53 W B, C M, L M. R s: - - ffi s. A M 2014;26:3484–9.

54 C H, W S, J , J, X , C J, S ff f F₃O₄ 2019;121:139–48.

55 W L, J, Q. T ff f MWCNTs s s. J M S : M E 2015;26(3):1895–9.

56 D , P GR, H P, Q F, M B , ML. Effi 2012;22:18772–4.

57 HB, Q, WG, H , .T - l ll 2011;3:918–24.

58 S A, U ll N, T l f V. T l f M f R 2016. s:// /10.1051/ f /2016021.

59 P s MT, J H, R ff RS, S L. T l s - s l f - s f f - l . N L 2012;12:2959–64.

60 J K, H, H , D . P f f - ll f f C -N ll - s s l s l f . M L 2017;122:244–7.

61 R H, L S, B S, K TW, L DS, L HJ, l T - s l s f . S R 2015. s:// /10.1038/s 12710. ss -

62 T, F SG, L , G Q, L G, R KP, l S s l X - s s s 3D s/ ll l f f . M S E A-S 2020. s:// /10.1016/j 2019.105670.

63 R DA, M LE, M E, H DH, M JL, M BI, l N l - s l f s l f s l . A s f s l l s f . J T s M 2011;59(10):4088–99.

64 E s SF, L KG, S s VK, M IC. T l l s f . J T s E l 1973;1(1):10–38.